arXiv:1403.6970v2 [cond-mat.mes-hall] 29 Mar 2014

Tight-binding simulations of electrically driven spin-valley transitions in carbon nanotube quantum dots

E. N. Osika, A. Mreńca, and B. Szafran
AGH University of Science and Technology,
Faculty of Physics and Applied Computer Science,
al. Mickiewicza 30, 30-059 Kraków, Poland
(Dated: April 1, 2014)

We describe the dynamics of the spin and valley transitions driven by alternating electric fields in quantum dots defined electrostatically within semiconducting carbon nanotubes (CNT). We use the tight-binding approach to describe the states localized within a quantum dot taking into account the circumferential spin-orbit interaction due to the s-p hybridization and external fields. The basis of eigenstates localized in the quantum dot is used in the solution of the time-dependent Schrödinger equation for description of spin flips and inter-valley transitions that are driven by periodic perturbation in the presence of coupling between the spin, valley and orbital degrees of freedom. Besides the first order transitions we find also fractional resonances. We discuss the transition rates with selection rules that are lifted by atomic disorder and the bend of the tube. We demonstrate that the electric field component perpendicular to the axis of the CNT activates spin transitions which are otherwise absent and that the resonant spin-flip time scales with the inverse of the electric field.

I. INTRODUCTION

Electron spins confined in carbon nanotube[1] (CNT) quantum dots[2] (QD) are considered attractive for quantum information storage and processing due to the absence of the hyperfine interaction[3] which is the main source of decoherence in III-V nanostructures. The spin-orbit (SO) coupling that is intrinsically present in CNTs due to s-p hybridization accompanying the curvature of the graphene plane[4–9] paves the way for electrical control of the confined carrier spins. In particular the SO interaction allows for spin flips induced by AC electric fields[10] according to the mechanism of the electric-dipole spin resonance as studied earlier for III-V quantum dots.[11–16]

In nanotube quantum dots the SO coupling splits the four-fold degeneracy of energy levels with respect to the spin and valley into Kramers doublets with spin-orbit coupling energy varying from a fraction of meV[8,17] to several meV.[18] In this work we study the states confined in a QD defined electrostatically within the CNT and simulate spin and valley transitions driven by AC electric field between the quadruple of nearly degenerate energy levels in external magnetic field.

For clean CNTs the coupling between the K and K' valleys is absent which motivates ideas to use the valley degree of freedom as a carrier of the quantum information alternative for the electron spin. In the transport experiments the valley filters and valves were proposed[19] for clean samples in which the inter-valley scattering can be neglected. For clean CNT double quantum dots the phenomenon of valley blockade has been demonstrated in experiment[20] and studied theoretically[21] as the equivalent of the Pauli spin blockade.[22] A theory for Rabi inter-valley resonance for CNT has also been presented[23] within a continuum approximation of the tight-binding Hamiltonian.

In the this work we report on time-dependent tight-binding simulations for the spin-valley transitions driven by AC field. In the present model the electron confinement within the dot, the lattice disorder, and the spin-valley dynamics are monitored at the atomic scale. We work with a direct solution to the time dependent Schrödinger equation which allows us to resolve not only the Rabi oscillations corresponding to the first order transition but also the fractional resonances in higher-order transitions observed in EDSR experiments on III-V[24] as well as CNT[20] QDs.

We discuss the effects driving the spin-flips with a particular focus on the electric field component that is perpendicular to the axis of the CNT, and which is bound to appear in experimental setups with CNTs deposited or suspended above the gates.[8,18,20] We show that a very similar dynamics of transitions is obtained for a bent CNT. An idea to exploit the bend of the nanotube to allow for electric dipole spin resonance in nanotubes was previously proposed[25] but in the context of the electron motion along the bend in the external magnetic field and the resulting variation of the effective Zeeman splitting. In the present system the motion of the electron is limited to the QD area and has a secondary effect on the transitions, still the bend of the nanotube in external *electric* field lowers the symmetry of the eigenstates which allows for the spin flips. We discuss the consequences of the perpendicular electric field, disorder and the bend of the CNT for selection rules and transition times.

II. MODEL

We consider a QD defined within a CNT by an external potential that is depicted in Fig. 1(a). The nanotube has a finite length $L = 21.16$ nm with a diameter of $2r = 1.56$ nm (after Ref. 26). The CNT is placed symmetrically within (x, z) plane with the external magnetic field ap-

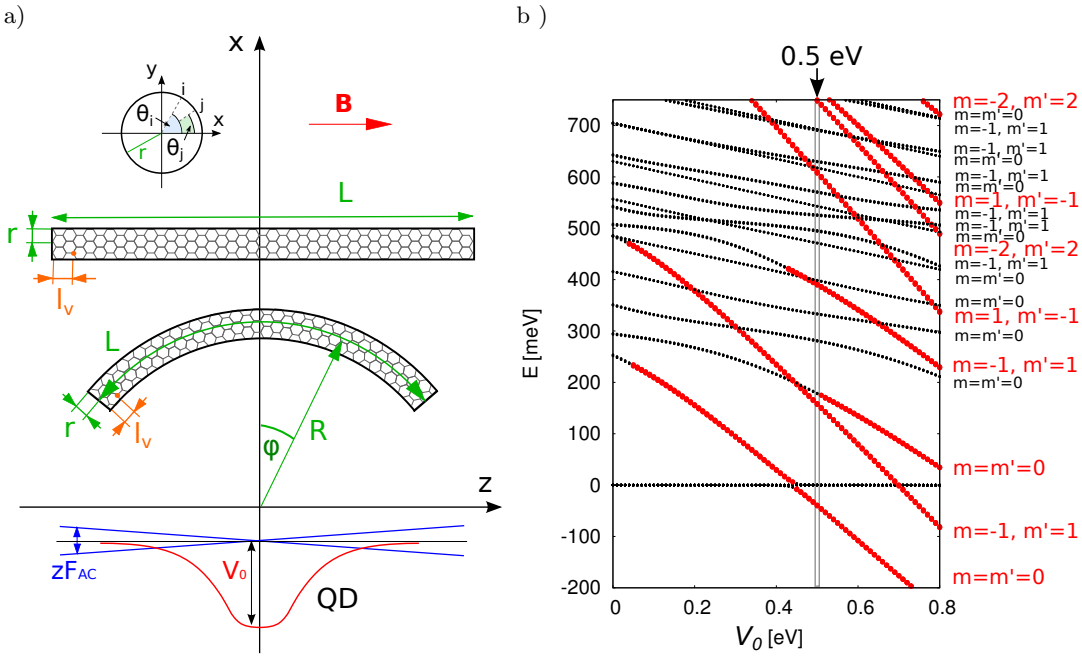

Figure 1: (a) Schematics of the considered system. In the top inset the definition of localization angles of carbon atoms at a cross section of the tube perpendicular to its axis is given. Below: a straight and bent CNT of length L and arc radius R. r is the radius of the nanotube and l_v is the distance of a vacant carbon atom removed in a part of calculations from the end of the tube. The bottom plot: the external confinement potential defining the QD and the potential due to AC field. (b) Energy spectrum for the finite nanotube in function of the depth of the Gaussian confinement potential. With the red dots we marked the energy levels with 50% of the probability density within the QD area ($[-d, d]$). On this scale of the plot the energy spectrum is indistinguishable for all the systems considered here (straight/bent with or without SO coupling, disorder etc.). On the right hand side of the figure the quantum numbers m (m') defining variation of the wave functions along the circumference of the nanotube for the states of valley K (K').

plied along the z axis. We model the external potential, induced e.g. by a gate electrode, of a Gaussian[28] form $W_{QD}(\mathbf{r}) = -V_0 \exp(-z^2/d^2)$, with $d = 0.1L$. In most of the simulations we take $V_0 = 0.5$ eV. We consider both a straight and bent CNT [see Fig. 1(a)]. For the latter we assume that the tube forms an arc of a radius $R = 20$ nm [see Fig. 1(a)]. In order to simulate the atomic disorder within the tube we assume that one carbon atom is missing within the lattice. In Fig. 1(a) l_v is the distance of the vacancy from the edge of the CNT. Whenever the vacancy defect is introduced we take $l_v = 0.85$ nm, i.e. fourth elementary cell from the edge of the tube. In the calculations the external magnetic field is applied along the z direction, unless stated otherwise.

We use the tight-binding Hamiltonian

$$H = \sum_{\{i,j\}} t_{ij}(c_i^\dagger c_j + c_j^+ c_i) + \sum_i \left(W_i + \frac{1}{2} g\mu_b \overrightarrow{\sigma} \cdot \overrightarrow{B} \right) c_i^\dagger c_i, \quad (1)$$

where the first summation runs over $2p_z$ spin-orbitals of nearest neighbor pair of atoms, $c_i^\dagger$ (c_i) is the particle creation (annihilation) operator at ion i, and t_{ij} is the hopping parameter. The second sum in Eq. (1) runs over all the $2p_z$ spin-orbitals where the term with the Landè factor $g = 2$ introduces the spin Zeeman splitting with $\overrightarrow{\sigma}$ standing for the vector of Pauli matrices. We found that inclusion of an external electric field perpendicular to the axis of the nanotube lifts the selection rules, in particular by influencing the wave functions dependence on θ [Fig. 1(a)]. This component of the electric field appears naturally when CNT is deposited above gates [cf. Refs. 8,18,20]. In this work we account for the linear electric field potential $W_x = eF_x x$. The local potential at the i-th ion W_i is taken as a superposition of the quantum dot potential and the potential due to perpendicular external electric field $W_i = W_{QD}(\mathbf{r}_i) + W_x(\mathbf{r}_i)$.

In the tight-binding Hamiltonian the spin-orbit coupling is introduced via the spin dependence to the hopping parameters t_{ij}.[4,34] The role of separate contributions to the spin-orbit coupling were discussed in detail in Ref. 5. The curvature induced coupling for the tube diameter of the order of 100 nm exceeds 3 times the Rashba SO coupling produced by the external electric field of 1600 kV/cm, i.e. of the order that is induced by the Gaussian potential assumed in this work. The curvature induced SO coupling energy is inversely proportional to the diameter of the nanotube.[5] For the diameter of the nanotube considered here we expect that the

curvature-induced SO coupling is by two orders of magnitude stronger than the one due to external fields, so we neglect the latter.The electric field that is perpendicular to the axis of the dot F_x is taken equal to 100 kV/cm. The resulting Rashba SO interaction is negligible.

The effects of CNT curvature including the spin-orbit coupling term are introduced following Refs. 4 and 7, with the hopping terms given by

$$\begin{aligned} t_{\uparrow\uparrow} &= \langle z_i\uparrow_z|H|z_j\uparrow_z\rangle = V_{pp}^{\pi}\cos(\theta_i-\theta_j) \\ &- (V_{pp}^{\sigma}-V_{pp}^{\pi})\frac{r^2}{a_C^2}[\cos(\theta_i-\theta_j)-1]^2 \\ &+ 2i\delta\big\{V_{pp}^{\pi}\sin(\theta_i-\theta_j)+ \\ &(V_{pp}^{\sigma}-V_{pp}^{\pi})\frac{r^2}{a_C^2}\sin(\theta_i-\theta_j)[1-\cos(\theta_i-\theta_j)]\big\} \end{aligned} \quad (2)$$

$$t_{\downarrow\downarrow} = \langle z_i\downarrow_z|H|z_j\downarrow_z\rangle = \langle z_i\uparrow_z|H|z_j\uparrow_z\rangle^* \quad (3)$$

$$\begin{aligned} t_{\uparrow\downarrow} &= \langle z_i\uparrow_z|H|z_j\downarrow_z\rangle = \\ &-\delta(e^{-i\theta_j}+e^{-i\theta_i})(V_{pp}^{\sigma}-V_{pp}^{\pi})\frac{rZ_{ji}}{a_C^2}[\cos(\theta_i-\theta_j)-1] \end{aligned} \quad (4)$$

$$t_{\downarrow\uparrow} = \langle z_i\downarrow_z|H|z_j\uparrow_z\rangle = -\langle z_i\uparrow_z|H|z_j\downarrow_z\rangle^*, \quad (5)$$

where z_i stands for $2p_z$ orbital on i-th atom, $\uparrow_z$ and $\downarrow_z$ indicate the orientation of the spin along the z direction, $V_{pp}^{\pi}=-2.66\,\text{eV}$, $V_{pp}^{\sigma}=6.38\,\text{eV}$,[27] $a_C=0.142$ nm is the distance between the nearest neighbor atoms, θ_i indicates the localization angle of atom i in the (x,y) plane [see the top inset in Fig. 1(a)], and $Z_{ji}=Z_j-Z_i$ is the distance between atoms i and j in the z direction. We adopt the SO coupling parameter $\delta=0.003$ after Refs. 4 and 7.

In the present model the spin-orbit interaction is uniquely due to the curvature of the graphene plane. Since the bend of the entire nanotube [Fig. 1(a)] is weak as compared to the graphene folding curvature ($R/r=20/0.78\simeq 25$) we do not take into account any extra spin-orbit interaction due to a finite value of R.

In presence of the external magnetic field the hopping parameters acquire an additional Peierls phase

$$t_{nm}\to t_{nm}e^{i2\pi\Phi_{nm}} \quad (6)$$

with the Aharonov-Bohm phase $\Phi_{nm}=(1/\Phi_0)\int_{r_n}^{r_m}\boldsymbol{A}\cdot\boldsymbol{dl}$, and the flux quantum $\Phi_0=h/e$.

The folding of the CNT is defined by the chiral vector $\boldsymbol{C_h}=n_1\boldsymbol{a_1}+n_2\boldsymbol{a_2}$, where $\boldsymbol{a_1}=a_0(1,0)$, $\boldsymbol{a_2}=a_0(1/2,\sqrt{3}/2)$ and $a_0=0.246$ nm [see Fig. 3]. In this paper we assume a zigzag CNT with $n_2=0$, which possesses a semiconducting character with the energy gap allowing for electrostatic confinement of the carriers provided that n_1 is not a multiple of 3.[1] In the following we take $n_1=20$ atoms along the circumference of the tube.

The spin-orbital eigenstates of Hamiltonian H, that are localized in the quantum dot induced by the external Gaussian potential are used for construction of the basis in which the EDSR is simulated,

$$\Psi(\boldsymbol{r},\sigma,t)=\sum_n c_n(t)\Psi_n(\boldsymbol{r},\sigma)e^{-\frac{iE_nt}{\hbar}}. \quad (7)$$

We consider the AC electric field that is applied along the nanotube, which introduces time dependence to the Hamiltonian

$$H'(t)=H+eF_0z\sin(\omega t), \quad (8)$$

with the amplitude of the oscillation taken equal to $F_0=4$ kV/cm and tunable frequency ω. The wave function (7) inserted to the time-dependent Schrödinger equation $i\hbar\frac{d\Psi}{dt}=H'\Psi$, upon projection on the basis of dot-localized H eigenstates gives a system of differential equations for the dependence of the expansion coefficients on time

$$i\hbar c_k'(t)=\sum_n c_n(t)eF_0\sin(\omega t)\langle\Psi_k|z|\Psi_n\rangle e^{-\frac{i(E_n-E_k)t}{\hbar}}, \quad (9)$$

which we solve for $c_k(t)$ using the implicit Crank-Nicolson scheme.

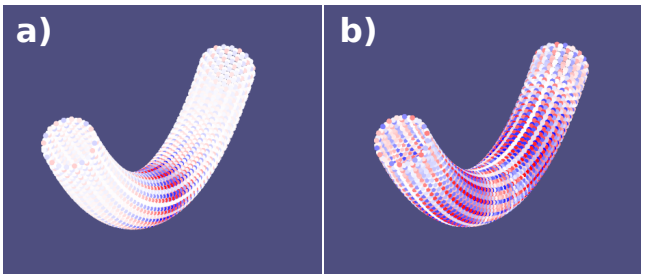

Figure 2: (a) The wave function of the lowest-energy QD localized level of Fig. 1(b) for $V_0=0.5$ eV of energy -40 meV. Real part of the majority (spin-up) component of the $m'=0$ wave function corresponding to K' valley. (b) Real part of the majority (spin-up) component of the $m'=0$ wave function corresponding to K' valley but delocalized with the energy of 280 meV [see Fig. 1(b)]. The values are given at the carbon atoms with red and blue colors corresponding to the opposite signs of the wave function.

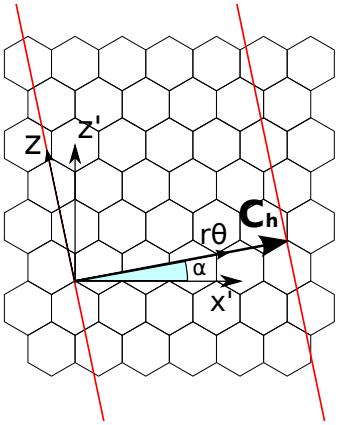

Figure 3: The chiral vector $\mathbf{C}_h$ defining the folding of the nanotube and system of the coordinates used in the text.

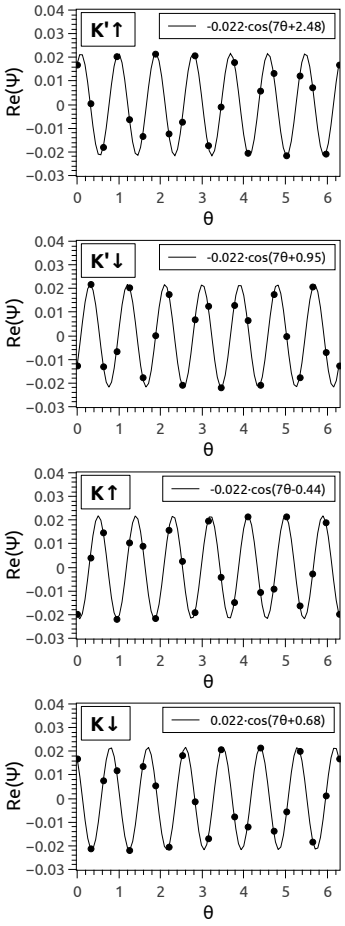

Figure 4: Real part of the spin majority part of the nearly degenerate lowest QD localized level of the energy $\simeq -40$ meV for $V_0 = 0.5$ eV. The dots indicate the values of the wave functions at the 20 atoms along the CNT circumference and the solid line indicates the wave function of the continuum approximation after Ref. 6.

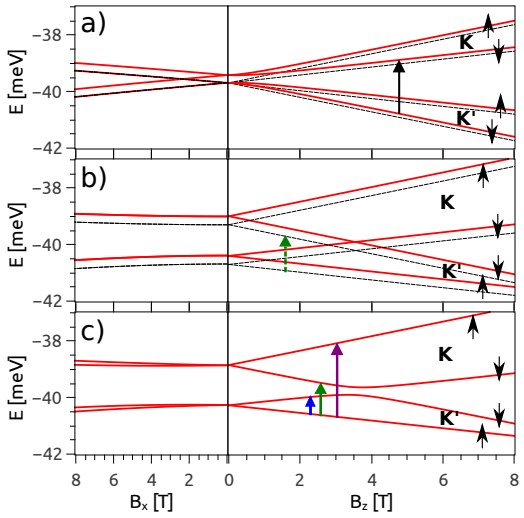

Figure 5: Energy spectrum for the lowest-energy QD localized electron energy level for $V_0 = 0.5$ eV as a function of the external magnetic field oriented along the x or z axis. In (a) a straight CNT is considered without SO coupling ($\delta = 0$). The black energy levels correspond to a CNT without disorder. The red energy levels were obtained for a vacant carbon atom (see Fig. 1 for location of the defect). (b) The energy spectrum with SO coupling ($\delta = 0.003$) for a straight CNT (red lines) and for a bent one (black lines). (c) Spectrum for a straight CNT with a vacancy [see Fig. 1(a)]. The vertical arrows in all the figures indicate the spin/valley transitions discussed in the text.

The low-energy continuum Hamiltonian for CNTs with spin-orbit coupling due to the curvature of the tube was derived in Ref. 9 from the tight-binding model with application to the electric-dipole spin resonance. The low-energy theory was also applied for demonstration of helical modes in CNTs.[29]

III. THE STATIONARY STATES

Figure 1(b) shows the energy spectrum of states within the nanotube in function of V_0 in the absence of the external magnetic field. At the scale of this figure, for all the considered cases (straight / bent nanotube, with or without vacancy, with or without a component of the electric field in the x direction) the spectrum is identical. The red lines indicate the energy levels with more than 50% of the probability density localized within the quantum dot. The zero energy level that is independent of V_0 is related to states localized at the Fujita edge of the CNT. We verified that the exact form of the edges at the end of the tube does not perturb the localized part of the spectrum. We find that the angular dependence of the localized states very well agrees with the continuum theory of Ref. 6. For nanotube with $(n_1, n_2) = (20, 0)$ that we consider here the angular dependence (fixed z) of the *majority* spin component of the eigenstates of the continuum Hamiltonian is of the form[6] $\Psi_n = A \exp(i(m \pm 7)\theta)$, where m is the angular quantum number, with $+$ for the K valley and $-$ for K' valley, and A standing for a constant that is independent of θ. At the scale of Fig. 1(b) all the energy levels appear as nearly four-fold degenerate with respect to the valley and the spin.[30–33]

Figure 4 shows the angular dependence of the real part of the lowest-energy electron QD confined states [the energy level marked in red with the energy of -40 meV for $V_0 = 0.5$ eV of Fig. 1(b)] as obtained with the tight-binding approach (dots) and a fit with the wave function of the continuum approximation.[6] We notice that all the states of these nearly degenerate energy levels correspond to $m = 0$. In a similar manner it is possible to identify the quantum numbers m for all the tight-binding wave functions within the nanotube, including the ones localized in the QD. The subsequent quantum numbers are given in Fig. 1(b) with primes for the K' valley.

Our identification of the valley is based on the en-

ergy dependence on the magnetic field along the CNT axis within the continuum approach for a rectangular potential defined within the CNT,[6] with $E_{m,k_n} = \pm\sqrt{(m+\frac{\Phi_{AB}}{\Phi_0}+\frac{1}{3})^2/r^2+k_n^2}$ for K valley (for K' valley one needs to replace m by m' and $\frac{1}{3}$ by $-\frac{1}{3}$) where $\Phi_{AB} = B\pi r^2$ and k_n are the discrete wave vectors corresponding to localization of the wave function within the quantum dot.[6] For $m = 0$ and $B > 0$ the K' (K) valley energy levels go down (up) in the energy.

The splitting of the lowest-energy electron level localized in the dot by the external magnetic field as obtained for the present model system is illustrated in Fig. 5. The panel (a) of Fig. 5 shows the spectrum without SO coupling for a straight CNT without disorder (black lines) and with the vacancy at 0.84 nm from the edge of the tube (red lines). For the magnetic field perpendicular to the axis of the dot one obtains energy level splitting by the spin Zeeman effect only. The field along the axis splits also the valley degeneracy. The coupling of the valleys introduced by the vacancy splits the energy level at $B = 0$. When the SO coupling is accounted for [Fig. 5(b)] the spectrum for $B = 0$ is split to spin-valley doublets[8] even without disorder. The spin-valley doublets are only split by the field along the z direction. The impact of the CNT bent [dark lines in Fig. 5(b)] to the spectrum is weak – there is a small shift to lower energies – mostly due to the fact that the bend introduces more carbon atoms within the QD area. When the vacancy is introduced [Fig. 5(c)] the coupling of the valleys produces avoided crossing between K and K' energy levels with spins oriented antiparallel to the magnetic field vector. The vertical arrows in Fig. 5 indicate the spin-valley transitions which are observed in the AC electric field and which are discussed below.

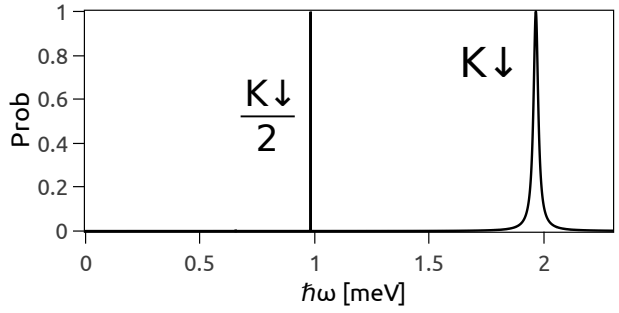

Figure 6: Results for the straight CNT without SO coupling but with a vacancy [cf. red lines in Fig. 5(a)] in the carbon lattice. We plot the maximal occupation of the $K\downarrow$ energy level for simulations lasting 500 ns starting from the $K'\downarrow$ ground-state as a function of the AC driving frequency ω.

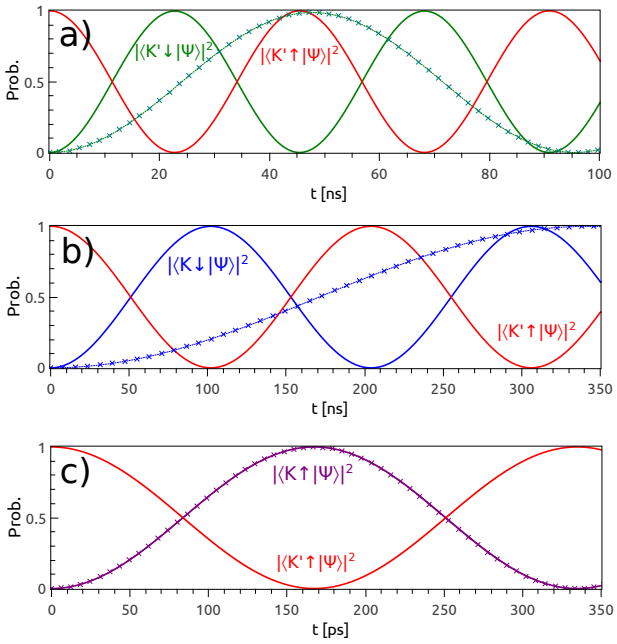

Figure 7: Time evolution for a straight CNT with SO coupling and a vacancy present within the system (the line marked with crosses). The solid lines without crosses correspond to results with an additionally introduced electric field of $F_x = 100$ kV/cm in the direction perpendicular to the axis of the system. The resonant frequencies were set for transitions from the ground state $K'\uparrow$ to $K'\downarrow$ (a) [spin flip – see the green arrow in Fig. 5(c)], $K\downarrow$ (b) [spin flip with inter-valley transition – the blue arrow in Fig. 5(c)], and $K\uparrow$ in (c) [inter-valley transition – the purple arrow in Fig. 5(c)]. The figures show the probabilities to find the system in the initial and final f state $|\langle\Psi(\boldsymbol{r},\sigma,t)|K'\uparrow\rangle|^2$ and $|\langle\Psi(\boldsymbol{r},\sigma,t)|f\rangle|^2$ of the resonant transition.

IV. SPIN-VALLEY TRANSITIONS

For simulations of the spin-valley transitions we set the external magnetic field along the z direction with $B = 5$ T. The time evolution in AC field is started from the lowest-energy state. In presence of SO coupling [see Fig. 5(b,c)] the ground state at $B_z = 5$ T is the spin-up state of K' valley. Naturally with SO and valley-orbit coupling present the designates of valley and spin are approximate and not strict. For still higher B there is a spin transition in the ground state for a higher magnetic field which is outside the Figure.

A. CNT without SO coupling

In the absence of SO coupling [see Fig. 5(a)] the spin-down ground-state is promoted by arbitrarily weak magnetic field. For the CNT without the vacancy [black lines in Fig. 5(a)] the system does not respond to AC field driving transition from the ground-state to any of the energy levels given in the figure, which are of a differ-

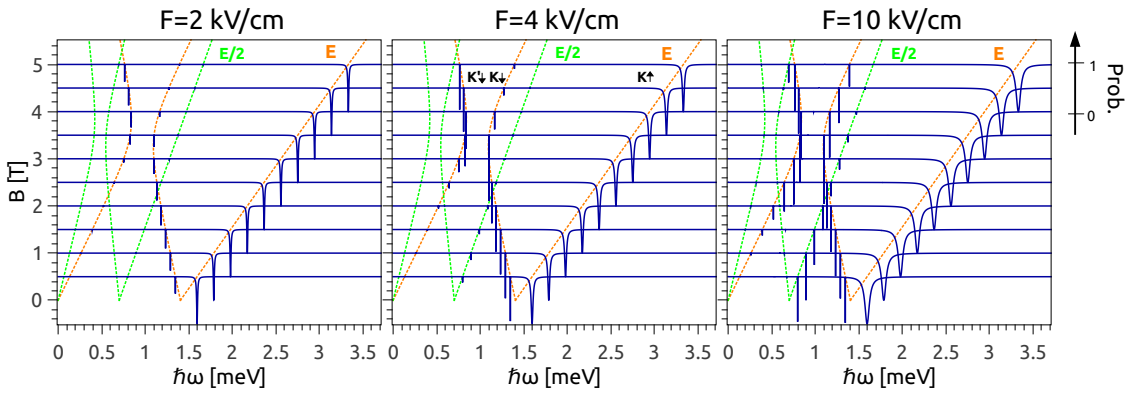

Figure 8: The orange lines show the energy spectrum calculated with respect to the ground state, i.e. the direct transition energies from the $K' \uparrow$ energy level. The green ones show half of the direct transition energies. The dark blue lines plot the minimal occupation probability of the ground state (initial one for the simulation) calculated with spacing of 0.5 T. Each simulation lasted 20 ns.

ent valley and/or opposite spin. For the CNT including the vacancy [energy levels marked in red in Fig. 5(a)] we do observe an inter-valley transition with conserved spin. The scan of the driving frequencies for these valley transitions is given in Fig. 6. In Fig. 6 we plot the maximal value of $|\langle\Psi(\boldsymbol{r},\sigma,t)|K\downarrow\rangle|^2$ that is obtained during 500 ns time evolution of the system. Besides the direct (first-order) transition near $\hbar\omega = 2$ meV, which was previously studied by the continuum approximation to the CNT without SO coupling but with phenomenologically introduced disorder[23] we find the fractional one at half of the basic frequency for the direct transition.

B. Straight CNT with SO coupling with disorder

We introduced the SO coupling to the straight CNT still with a vacancy present and in Fig. 7 we plotted the dynamics of transitions from the ground-state $K' \uparrow$ to the three other energy levels of Fig. 5(c). For each of the plots: the valley transition [Fig. 7(c)], the spin flip [Fig. 7(a)] and the transition including both valley and spin [Fig. 7(b)] we set the external frequency to the resonant one. The lines with (without) the crosses in Fig. 7(b) were obtained in the absence (presence) of the external field $F_x = 100$ kV/cm. This field has no detectable effect on the energy spectra of Fig. 5(b,c). Still its effect on transitions involving spin-flip [Fig. 7(a,b)] is distinct and it relies on shortening the transition time two to three times. The electric field applied in the x direction has no effect on the fast inter-valley transition [Fig. 7(c)], which is by two orders of magnitude shorter than the spin flip with preserved valley [Fig. 7(a)] and by three orders of magnitude shorter than the transition involving change of both the valley and the spin [Fig. 7(c)].

Figure 8 shows the transition energy spectrum and the transition effectiveness for the straight CNT including the electric field in the x direction for various amplitudes of the AC field. Orange lines correspond to direct transitions and the green ones to resonances at half of the basic frequency for the direct transitions. The duration of every simulation was set to 20 ns only. For the weakest amplitude ($F = 2$ kV/cm) we see the pronounced inter-valley transition with preserved spin [same as in Fig. 7(c)]. The other line that is observed is the spin-flip transition with preserved valley. The line with both spin and valley transition is only detectable at the avoided crossing between the valley states. For $F = 4$ kV/cm the traces of the half resonant inter-valley transition appear. For $F = 10$ kV/cm the half-resonant transitions are intensified. Note that the half resonance for low B is more effective than the direct inter-valley transition with spin flip. The half-resonant the inter-valley transition is less effective for higher B.

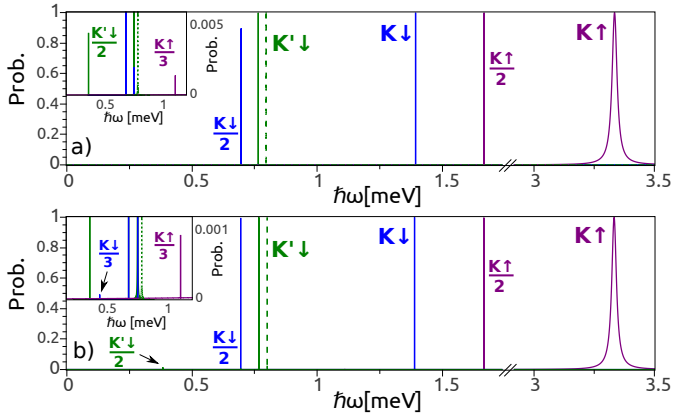

Figure 9: Same as Fig. 6 only with SO coupling for a straight (b) or bent (b) CNT. The inset shows the half resonances at the lower energy side. Solid (dashed) lines indicate the transitions with (without) a vacancy. In (a) the electric field in the x direction is present.

C. Bent CNT

The scan of the transitions in the evolution lasting 500 ns for the system corresponding to Fig. 8 [straight CNT with a vacancy and $F_x = 100$ kV/cm] is displayed in Fig. 9(a). When the disorder is present within the lattice the electric field perpendicular to the axis of the CNT only shortens the transition times [see Fig. 7] and does not open any new transition channels. The perpendicular electric field can be replaced by the bend of the disordered nanotube with no difference for the transitions – see the results of Fig. 9(b) (scan with the bend, a vacancy present and $F_x = 0$). When the disorder is removed we obtain only the direct spin-flip transition with preserved valley and its fractional resonances – see both panels of Fig. 9 for the dashed lines obtained the spin-flip direct and fractional transitions with preserved valley.

For perfectly ordered lattice and straight CNT, without the component of the electric field perpendicular to the tube axis *we do not* find *any* transitions in the considered energy range in spite of the presence of the SO coupling.

D. Transition times and selection rules

Summary of the direct transition times is given in Table I with spin-flip in the second column, spin-valley transition in the third column, and valley transition with conserved spin in the last column. The SO coupling due to the curvature of the nanotube is not enough to allow for spin transitions induced by AC field. The spin transitions do appear when additionally *(i)* a disorder is present or *(ii)* electric field perpendicular to the axis is present or *(iii)* the CNT is bent in the QD region occupied by electrons. The presence of the disorder alone for a CNT with SO coupling is enough do drive all the three types of transitions. Without disorder the bend and the perpendicular electric field only drive the spin flips and not the inter-valley transitions. The inter-valley transition when allowed by the presence of the disorder is much faster than transitions including spin-flips. The spin-flips (second column) that are present without disorder appear much faster when the disorder is introduced.

The time dependence of Fig. 7 for resonant frequencies indicate a pure two-level Rabi oscillation. In agreement with the Rabi mechanism we find that the transition times of Table I are inversely proportional to the absolute value of the matrix element $\langle i|z|f\rangle$, with i and f standing for the initial and final states. This matrix element also determines the selection rules of the discussed transitions. Let us consider the straight and clean nanotube, for which no spin-flip transition is observed in spite of the presence of the SO coupling. The spin-up and spin-down components of the integrands of the matrix element are given in Fig. 10. We find that the integrand function vanishes upon integration over the angle θ. The majority components of all the states considered in the

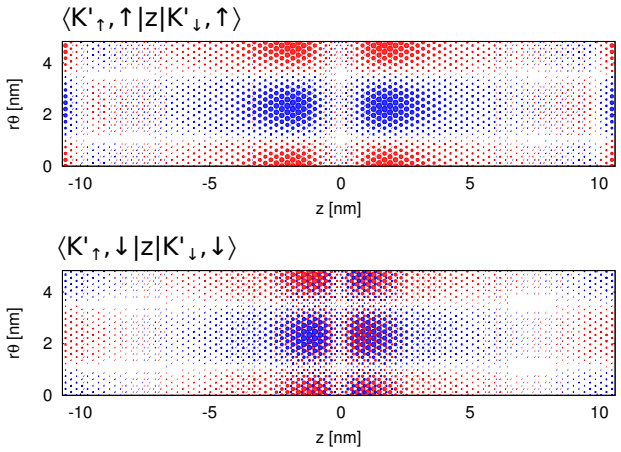

Figure 10: The real part of spin-up and spin-down components of the integrand for $\langle K' \uparrow |z| K' \downarrow\rangle$ matrix element. In the upper (lower) panel we plot the product of the majority (minority) spin component for the initial state and minority (majority) spin component of the finial state. The blue / red dots correspond to positive (negative) values.

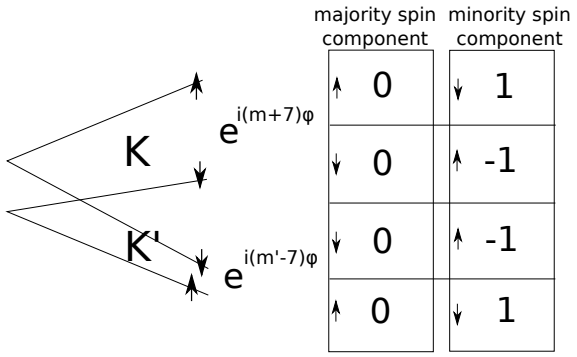

Figure 11: The angular quantum numbers m and m' for the majority and minority spin components for a straight and clean CNT. The numbers are given according to the order of energy levels at the right end of the schematically drawn spectrum.

context of the spin-valley transitions correspond to quantum number $m = m' = 0$ (see the discussion of Fig. 4). The calculation of the matrix element for the spin-flip involves products of the majority components of the initial state with the minority components of the final state, and vice versa. We extracted the quantum numbers for the minority spin components with the procedure explained in the context of Fig. 4 with the results summarized schematically in Fig. 11. The minority components differ by ± 1 from the majority ones, hence the orthogonality over the angle which leads to the absence of the spin-flip transitions for the straight and clean CNT. In order to allow for the transition that are forbidden by the angular symmetry to occur one needs to lift the symmetry of the CNT along the circumference. The electric field of about 100 kV/cm perpendicular to the axis or the bent of

	$\|K'\uparrow\rangle \to \|K'\downarrow\rangle$	$\|K'\uparrow\rangle \to \|K\downarrow\rangle$	$\|K'\uparrow\rangle \to \|K\uparrow\rangle$
straight CNT no vacancy $F_x = 0$	∞	∞	∞
straight CNT no vacancy $F_x = 100$ kV/cm	31 ns	∞	∞
straight CNT with vacancy $F_x = 0$	48 ns	342 ns	167 ps
straight CNT with vacancy $F_x = 100$ kV/cm	23 ns	102 ns	167 ps
bent CNT no vacancy $F_x = 0$	42 ns	∞	∞
bent CNT with vacancy $F_x = 0$	24 ns	114 ns	176 ps
	$\|K'\downarrow\rangle \to \|K'\uparrow\rangle$	$\|K'\downarrow\rangle \to \|K\uparrow\rangle$	$\|K'\downarrow\rangle \to \|K\downarrow\rangle$
straight CNT with vacancy, no SO	∞	∞	168 ps

Table I: Direct transition times from the lowest-energy QD-localized level at 5 T with spin flip (second column), spin-valley transition (third column) and valley transition (last column). Spin-orbit coupling is included in all the cases but the last row. In each a different driving frequency ω of AC field tuned to resonance was applied. The amplitude of AC field along the z axis was set to 4 kV/cm.

the nanowire allows for the spin-flip transition (see Fig. 12). The bend of the CNT is effective in activating the transitions because of its interplay with the Gaussian potential forming the QD [W_{QD}] which as due to external potential depends on z only and ignores the deformation of the CNT. In consequence at the bent part of the tube the atoms at the circumference perpendicular to the axis occupy locations with different potentials. The selection rules are restored when the radius of the arc increases: we found that the transition times for the spin-flip of a clean CNT scale linearly with R [Fig. 14(a)]. On the other hand for straight CNT the spin-flip time scales as an inverse of the perpendicular electric field [Fig. 14(b)].

Note, that for both the straight and clean CNT the states of opposite valleys with $m = \pm m'$ remain orthogonal by the angular dependence. In particular for $m = m' = 0$ for the considered zig-zag CNT with 20 atoms along the circumference the angular dependence is $\exp(i7\phi)$ and $\exp(-i7\phi)$ for both valleys. In terms of the transition matrix elements this results in the absence of the inter-valley transition for a clean CNT.

The disorder due to the vacancy near the end of the straight CNT perturbs not only the angular dependence [see Fig. 13] but also introduces asymmetry of the integrands with respect to the center of the QD.

For completeness in Fig. 14(d) we plotted the spin-flip transition times in function of the radius of the straight semiconducting CNTs. In this plot the value of the perpendicular electric field is changed for different r to keep the fixed potential difference at the opposite sides of the CNT. Electric field applied to the CNT of radius r is given by $F_x = 100$ kV/cm $\cdot$ (0.78 nm/r). We found that the time scales exponentially with the radius of the CNT, in spite of the fact that SO coupling energy decreases with r see Fig. 14(c). The symmetry breaking effect of the perpendicular electric field is stronger for larger r even at a constant potential difference across the CNT. The fact that SO is reduced with r does not prevent faster transition times for larger r. Note that the spin-transitions are forbidden even for strong SO interaction unless the angular symmetry is broken. In Fig. 14(c,d)

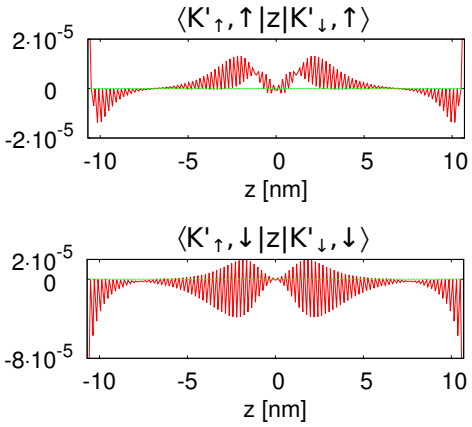

Figure 12: Same as Fig. 10 only integrated over the angle θ. The green (red) curve correspond to the straight and clean CNT and $F_x = 0$ ($F_x = 100$ kV/cm)

.

we found that the results are organized in two series depending on the number of the atoms on the circumference of the CNT with $N = 3i+\nu$, with i being an integer. The SO energy scales as $1/r$ for $\nu = 1$, for $\nu = -1$ at higher values of r the SO coupling energy vanishes slower.

V. SUMMARY AND CONCLUSIONS

In summary, we presented simulations of the spin flip and inter-valley transitions in a quantum dot defined within a semiconducting carbon nanotube. We considered a single excess electron in the quantum dot and evaluated the dynamics of the spin and valley transitions driven by external AC electric field. Time-dependent calculations used the basis of localized eigenstates as determined by the tight-binding approach.

For a straight and clean CNT the spin-flips are forbidden even for strong SO coupling. The spin transitions are triggered by electric field perpendicular to the axis of

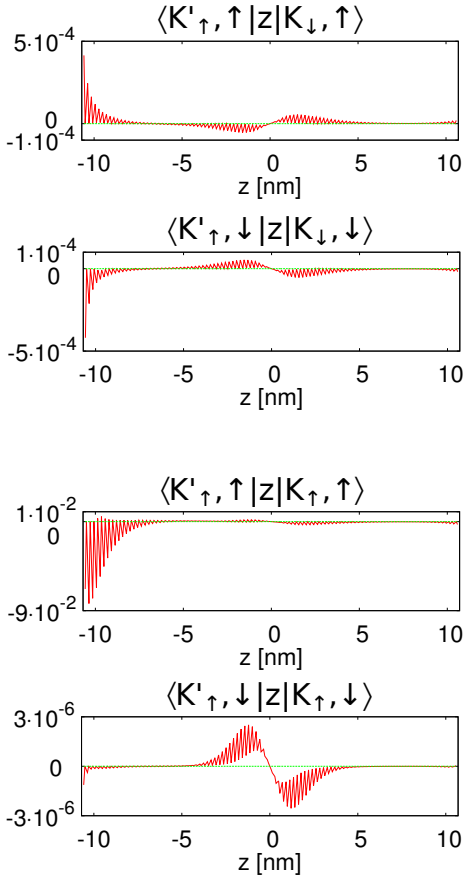

Figure 13: Components of the integrands for the transition matrix element for a straight CNT with a vacancy near the left end of the tube [see Fig. 1(a)].

the CNT. We demonstrated that the spin-flip transition times are inversely proportional to the value of the perpendicular electric field component. We demonstrated that the bend of the CNT in external electric field allows for the spin-flips due to lifting of the selection rules by lowering the angular symmetry of the eigenstates with the spin-flip transition times scaling linearly with R.

We demonstrated that when SO coupling is present the atomic disorder alone allows for all types of transitions including spin flips. We discussed the disorder introduced by a vacancy, which even when far from the QD perturbs the angular symmetry of the eigenstates lifting the selection rules prohibiting the inter-valley transitions. The inter-valley transitions when allowed by the lattice disorder appear roughly 100 to 1000 times faster than the spin flips and are insensitive to the electric fields perpendicular to the axis of the CNT.

Acknowledgements

This work was supported in part by Ministry of Science and Higher Education within statutory tasks of the Faculty and by the PL-Grid Infrastructure. Calculations

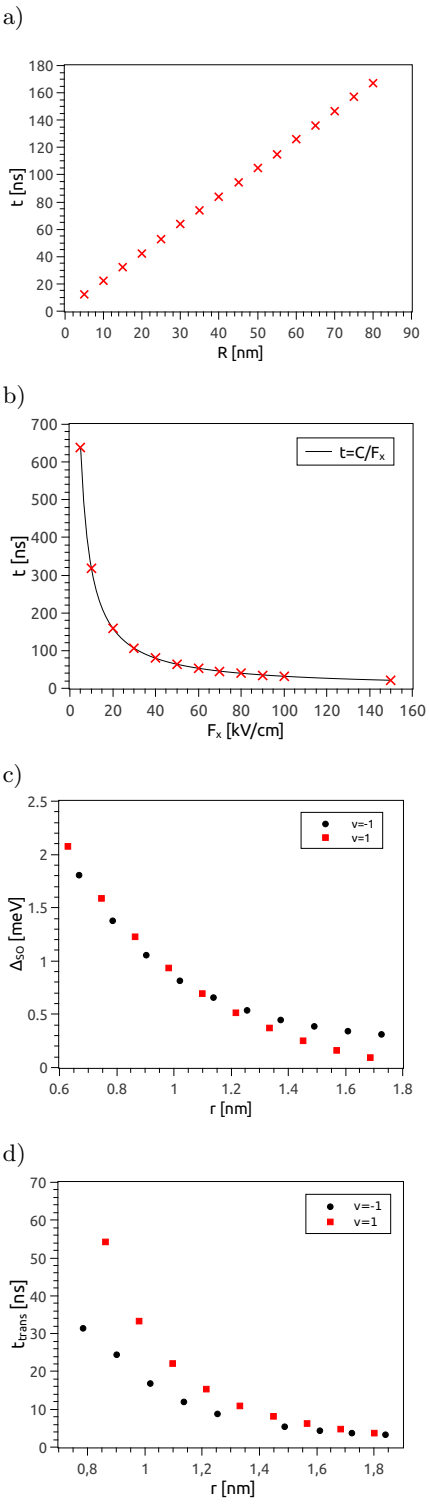

Figure 14: (a) Spin-flip transition $|K'\uparrow\rangle \rightarrow |K'\downarrow\rangle$ times as a function of the radius of the bent for a clean CNT for $B = 5$ T and AC amplitude of 4 kV/cm for $r = 0.78$ nm (as everywhere else in this paper) (b) Same as (a) only for a straight CNT in function of the electric field perpendicular to the axis of the CNT. (c) SO energy, i.e. the splitting of the Kramers doublets at $B = 0$, in function of the radius of the CNT for the straight and clean CNT without external fields. (d) Same as (b) only in function of the radius of the CNT. Here the value of the perpendicular electric field was changed to keep the potential difference at the opposite sides of the CNT constant i.e. $F_x = 100$ kV/cm $\cdot$ (0.78 nm $/r$).

were performed in ACK – CYFRONET – AGH on the RackServer Zeus.

[1] J. C. Charlier, X. Blase, and S. Roche, Rev. Mod. Phys 79, 677 (2007).

[2] S. Sapmaz, P. Jarillo-Herrero, L. P. Kouwenhoven and H. S. J. van der Zant, Semicond. Sci. Technol. **21** S52 (2006).

[3] H. O. H. Churchill, F. Kuemmeth, J. W. Harlow, A. J. Bestwick, E. I. Rashba, K. Flensberg, C. H. Stwertka, T. Taychatanapat, S. K. Watson, and C. M. Marcus, Phys. Rev. Lett. **102**, 166802 (2009).

[4] T. Ando, J. Phys. Soc. Jpn. **69**, 1757 (2000).

[5] D. Huertas-Hernando, F. Guinea, and A. Brataas, Phys. Rev. B **74**, 155426 (2006).

[6] D. V. Bulaev, B. Trauzettel, and D. Loss, Phys. Rev. B **77**, 235301 (2008).

[7] M. del Valle, M. Margańska, and M. Grifoni, Phys. Rev. B **84**, 165427 (2011).

[8] F. Kuemmeth, S. Ilani, D. C. Ralph, and P. L. McEuen, Nature **452**, 448 (2008).

[9] J. Klinovaja, M. J. Schmidt, B. Braunecker, and D Loss, Phys. Rev. B **84**, 085452 (2011).

[10] E. A.Laird, F. Pei, and L. P. Kouwenhoven, Nature Nano. **8**, 565 (2013).

[11] K. C. Nowack, F. H. L. Koppens, Yu. V. Nazarov, and L. M. K. Vandersypen, Science **318**, 1430 (2007).

[12] J. R. Petta , A. C. Johnson, J. M. Taylor, E. A. Laird, A. Yacoby, M. D. Lukin, C. M. Marcus, M. P. Hanson, and A. C. Gossard, Science **309**, 2180 (2005).

[13] J. Stehlik, M. D. Schroer, M. Z. Maialle, M. H. Degani, J. R. Petta, arXiv:1312.3875 (2013).

[14] F. H. L. Koppens, C. Buizert, K. J. Tielrooij, I. T. Vink, K. C. Nowack, T. Meunier, L. P. Kouwenhoven, and L. M. K. Vandersypen, Nature (London) **442**, 766 (2006).

[15] S. Nadj-Perge, S. M. Frolov, E. P. A. M. Bakkers, and L. P. Kouwenhoven, Nature **468**, 1084 (2010).

[16] S. Nadj-Perge, V. S. Pribiag, J. W. G. van den Berg, K. Zuo, S. R. Plissard, E. P. A. M. Bakkers, S. M. Frolov, and L. P. Kouwenhoven, Phys. Rev. Lett. **108** 166801 (2012).

[17] T. S. Jespersen, K. Grove-Rasmussen, J. Paaske, K. Muraki, T. Fujisawa, J. Nygård, and K. Flensberg, Nature Physics **7**, 348 (2011).

[18] G. A. Steele, F. Pei, E. A. Laird, J. M. Jol, H. B. Meerwaldt, and L. P. Kouwenhoven, Nature Communications **4**, 1573, (2013).

[19] A. Rycerz, J. Tworzydło, C.W.J. Beenakker, Nature Physics **3**, 172 (2007).

[20] F. Pei, E. A. Laird, G. A. Steele, and L. P. Kouwenhoven, Nature Nano. **7**, 630 (2012).

[21] A. Pályi and G. Burkard, Phys. Rev. B **82**, 155424 (2010).

[22] M. R. Buitelaar, J. Fransson, A. L. Cantone, C. G. Smith, D. Anderson, G. A. C. Jones, A. Ardavan, A. N. Khlobystov, A. A. R. Watt, K. Porfyrakis, and G. A. D. Briggs, Phys. Rev. B **77**, 245439 (2008).

[23] A. Pályi and G. Burkard, Phys. Rev. Lett. **106**, 086801 (2011).

[24] J. Stehlik, M. D. Schroer, M. Z. Maialle, M. H. Degani, J. R. Petta arXiv:1312.3875; E. I. Rashba, Phys. Rev. B **84**, 241305 (2011); M. P. Nowak, B. Szafran, and F. M. Peeters, Phys. Rev. B **86**, 125428 (2012); E. N. Osika, B. Szafran, and M. P. Nowak, Phys. Rev. B **88**, 165302 (2013); G. Széchenyi, and A. Pályi, Phys. Rev. B **89**, 115409 (2014).

[25] K. Flensberg and C.M. Marcus, Phys. Rev. B **81**, 195418 (2010).

[26] S. H. Jhang, M. Margańska, Y. Skourski, D. Preusche, B. Witkamp, M. Grifoni, H. van der Zant, J. Wosnitza, and C. Strunk, Phys. Rev. B **82**, 041404(R) (2010).

[27] D. Tománek and S. G. Louie, Phys. Rev. B 37, 8327 (1988).

[28] J. Adamowski, M. Sobkowicz, B. Szafran, and S. Bednarek, Phys. Rev. B **62**, 4234 (2000).

[29] J. Klinovaja, M. J. Schmidt, B. Braunecker, and D. Loss, Phys. Rev. Lett. **106**, 156809 (2011).

[30] D. H. Cobden, and J. Nygård, Phys. Rev. Lett. **89**, 046803 (2002).

[31] W. Liang, M. Bockrath, H. Park, Phys. Rev. Lett. **88**, 126801 (2002).

[32] P. Jarillo-Herrero, J. Kong, H. S. J. van der Zant, C. Dekker, L. P. Kouwenhoven, and S. De Franceschi, Phys. Rev. Lett. **94**, 156802 (2005).

[33] S. Moriyama, T. Fuse, M. Suzuki, Y. Aoyagi, and K. Ishibashi, Phys. Rev. Lett. **94**, 186806 (2005).

[34] L. Chico, M. P. López-Sancho, and M. C. Muñoz, Phys. Rev. Lett. **93**, 176402 (2004).